Measurements with the Chandra X-Ray Observatory's flight contamination monitor

R. F. Elsner, J. J. Kolodziejczak, S. L. O'Dell, D. A. Swartz, A. F. Tennant and M. C. Weisskopf

NASA Marshall Space Flight Center, SD50
Huntsville, AL 35812 USA

ABSTRACT

NASA's *Chandra* X-ray Observatory includes a Flight Contamination Monitor (FCM), a system of 16 radioactive calibration sources mounted on the inside of the Observatory's forward contamination cover. The purpose of the FCM is to verify the ground-to-orbit transfer of the *Chandra* flux scale, through comparison of data acquired during the ground calibration with those obtained in orbit, immediately prior to opening the Observatory's sun-shade door. Here we report results of these measurements, which limit the absolute value of the change in mirror-detector system response to less than 2% at Ag Lα ($\sim$ 3 keV) and Mn Kα ($\sim$ 6 keV). This limit is consistent with the prelaunch estimate of less than 10 $\AA$ accumulation of molecular contamination between ground calibration and initial on-orbit operations.

Keywords: *Chandra*, space missions, x rays, grazing-incidence optics, calibration, contamination, x-ray missions.

1. INTRODUCTION

The *Chandra* X-ray Observatory, the x-ray component of NASA's Great Observatories launched in July 1999,[1] underwent the most extensive system-level calibration program in the history of high-energy astrophysics. Consucted at the Marshall Space Flight Center (MSFC) X-Ray Calibration Facility (XRCF) during the winter and spring of 1997,[2] one of the key goals of the calibration was to determine the absolute flux scale to an accuracy of a few percent or less. Using a high-fidelity ray-trace program, maintained by the *Chandra* Mission Support Team at the Smithsonian Astrophysical Observatory (SAO), detailed analysis of effective area measurements taken at XRCF has achieved this goal.[3] However, it is still important to verify the transfer of the ground-level calibration to on-orbit operation, particularly in view of the absence of any well characterized astronomical x-ray standard candles and the sensitivity of the *Chandra* effective area to changes in molecular and particulate contamination[4] (Fig. 1).

For these reasons, a Flight Contamination Monitor system (FCM), comprising electron-capture radioactive sources emitting x-ray lines, resides in the Forward Contamination Cover (FCC) of the HRMA (Fig. 2). There are four sources, spaced 90^o apart, for each HRMA shell, with activities and radii scaled appropriately for that shell's geometric aperture. The two objectives of the ground and in-orbit measurements using the FCM and focal-plane detectors are these:

(1) Verify the transfer of the HRMA absolute flux scale from the XRCF test phase to the orbital activation phase (OAC).

(2) Measure or bound any changes in molecular contamination of the HRMA.

The focal-plane detectors, the Advanced CCD Imaging Spectrometer (ACIS) and the High-Resolution Camera (HRC), also employ their own radioactive calibration sources, in order to monitor any change in detector performance. The ground calibration included FCM measurements with ACIS, ACIS-2C (an ACIS surrogate),

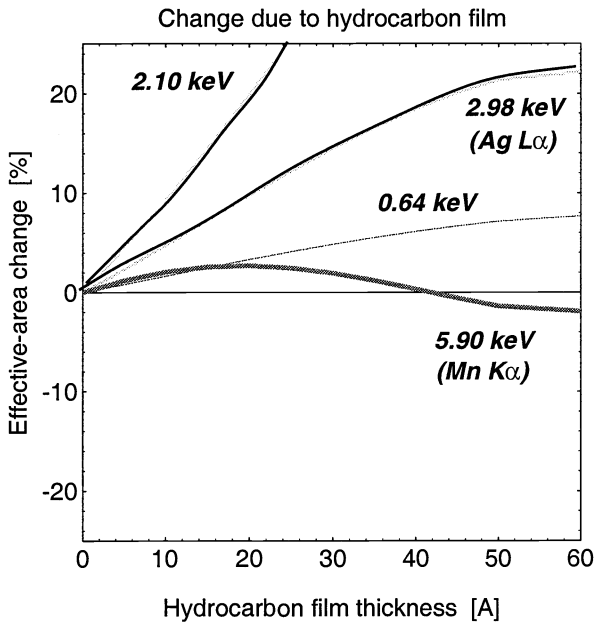

Figure 1. *Chandra* effective area changes in percent, at selected x-ray energies, as a function of the thickness of a uniform hydrocarbon film over 95% bulk density iridium.

Contact information:
R.F.E.: elsner@avalon.msfc.nasa.gov; 256-544-7741.

X-Ray Optics, Instruments, and Missions IV, Richard B. Hoover, Arthur B. C. Walker II, Editors,
Proceedings of SPIE Vol. 4138 (2000) © 2000 SPIE. · 0277-786X/00/$15.00

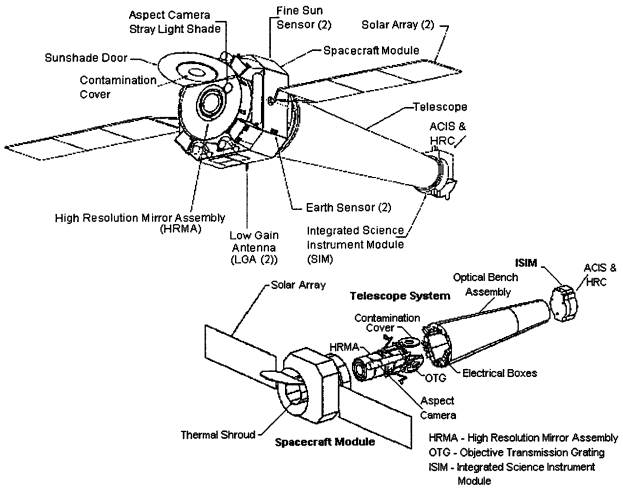

Figure 2. The *Chandra* spacecraft and components showing the FCC on the front of the HRMA. FCM measurements are taken during the activation phase with the FCC closed.

and HRC-I (the imaging readout for HRC). On-orbit FCM measurements during the activation phase used only ACIS and were the first look at the on-orbit HRMA/ACIS performance. Figure 3 is a schematic of the x-ray optical path for FCM measurements.

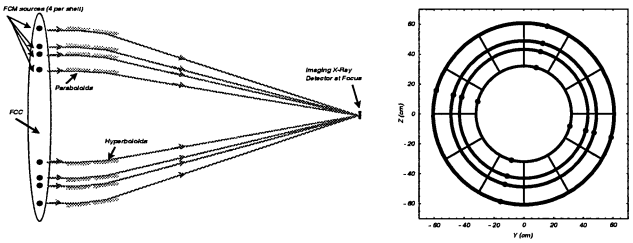

Figure 3. Left: The x-ray optical path for FCM measurements showing the FCM sources in the FCC, reflections off the paraboloids and hyperboloids of the four HRMA mirror shells, and collection by a focal plane detector (ACIS and, on the ground only, ACIS-2C and HRC-I). Right: Positions of the FCM sources projected on the paraboloid apertures midway between support struts for the baffle plates in the thermal pre-collimator, central aperture plate, and thermal post-collimator.

Each FCM source illuminates the portion of the paraboloid aperture immediately in front of it, leading to an image of a slightly curved stripe in the focal plane. The FCM source 180^o away contributes a stripe superimposed on the first one, but with a slight curvature in the opposite direction. The pair of FCM sources at 90^o with respect to the first two contribute stripes perpendicular to the first two, leading to an image of a cross in the focal plane (Fig. 4). Although the global topology of the image is independent of energy, intensity contours depend slightly on energy, due to the differing energy response of the four HRMA shells. Cross-correlation of measured and simulated images provides a measure of any FCC position shifts (§4).

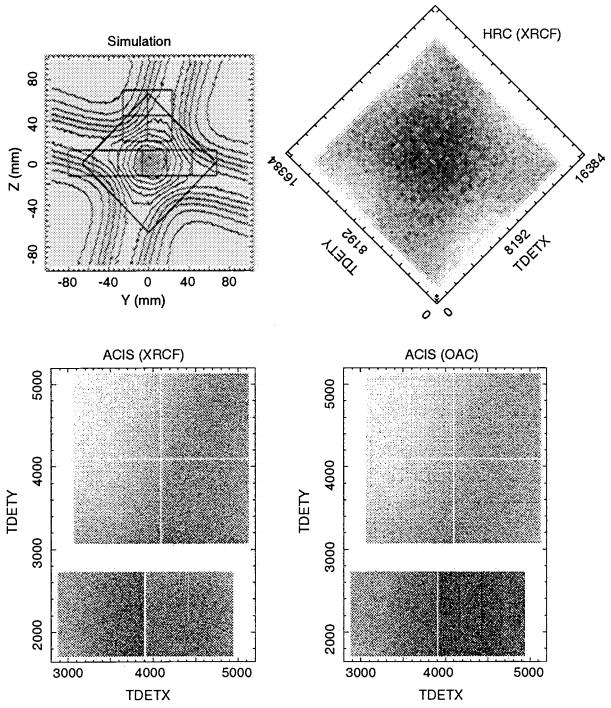

Figure 4. FCM images. The simulated image in the top left panel shows the cross pattern generated in the focal plane by the FCM system, with outlines of the focal-plane detectors ACIS and HRC-I superimposed. The Y and Z axes are perpendicular to the optical axis and lie in the dispersion and cross-dispersion directions. The top right panel shows the XRCF HRC-I image, in HRC detector coordinates. The bottom panels show ACIS FCM images (for ASCA grades 0, 2, 3, 4, and 6) at XRCF (left) and OAC (right), in ACIS detector coordinates. (CCD grades reflect the distribution of detected charge and are useful for sorting real x-ray events from charged-particle tracks.)

Ideally, direct comparison of ground and on-orbit FCM measurements at as many lines as possible would provide a direct transfer of the absolute flux scale from XRCF to orbit, or would provide direct measures of any discrepancies. In practice, some modeling is necessary, due to several factors: Differing HRMA/ACIS orientation at XRCF and OAC; the different gravity and thermal environments at XRCF and on-orbit; radioactive decay; different particle backgrounds and ACIS operating temperatures; and possible changes in relative FCM, FCC

and HRMA positions (for example, due to launch vibrations). Finally, interpretation of any discrepancies with the HRMA model derived from the ground calibration requires ray-trace simulations, for which we use the Project Science ray-trace code.

In this paper, we first describe the characterization of the flight FCM radioactive sources (§2) and the spectral analysis of FCM measurements taken at XRCF and during OAC (§3). Next we discuss the registration analysis necessary to determine any positional shifts of the FCC relative to its nominal position (§4), and the differences in FCM rates between XRCF and OAC predicted by our ray-trace simulations, as well as sources of systematic errors (§5). Finally we compare the XRCF and OAC measurements with each other and with ray-trace simulations, concluding that any difference in HRMA throughput between XRCF and OAC is less than 2 % (§6).

2. RADIOACTIVE SOURCES

The FCM comprises sixteen (one per shell per quadrant) electron-capture sources positioned midway between support struts (Fig. 3). The radioactive sources contain ^{109}Cd and ^{55}Fe prepared at Isotope Products, Inc., packaged by MSFC, and mounted on the FCC. To prevent leakage, MSFC had to seal each source assembly with a 100-μm-thick Be window. MSFC measured the individual FCM flight source activities (Table 1), with corroborating measurements by the US Army Redstone Arsenal. Dominated by systematic effects, the estimated errors in the measured absolute activities are about 15%. However, activity ratios between sources are known with significantly higher precision than the absolute activities. Statistical uncertainties (1σ) in the ^{55}Fe activities, derived from measurements of the Mn Kα line strength, range from 0.2% (shell 1) to 0.4% (shell 6). Statistical uncertainties (1σ) in the ^{109}Cd activities, derived from measurements of the Ag Kα (22 keV) line strength, range from 0.04% (shell 1) to 0.1% (shell 6). However, the lower energy ($\approx$3 keV) lines in the Ag L series are significantly affected by the overlying material in the source assemblies. The internal configuration, from the substrate up, is ^{109}Cd ($\sim$0.3 μm), a gold buffer layer ($\sim$0.05 μm), ^{55}Fe ($\sim$0.1 μm), a gold sealing layer ($\sim$0.05 μm), and finally the beryllium window (100 μm). These layers absorb $\sim$60% of the 3-keV Ag-L series x rays emitted from the ^{109}Cd. The range over which the actual layer thicknesses vary about their nominal values is unknown. MSFC measured the spatial uniformity of all FCM sources at 22, 6, and 3 keV. Figs. 6 and 7 show examples of the ^{109}Cd and ^{55}Fe uniformity maps. The *Chandra* Project Science ray-trace code takes into account these spatial variations.

Ray-trace simulations for the registration analysis (§ 4 below) use the activities given in Table 1. The radioactive half-lives of ^{109}Cd and ^{55}Fe are 1.2641$\pm$0.0033 and 2.73$\pm$0.02 yr,[5] respectively; so compensation for radioactive decay is necessary in the data analysis.

Table 1. Nominal FCM source activities (mCi) on 1997 Mar 5[a] and radii R (mm).

	1	3	4	6
-15	4.03,1.20	2.44,0.73	1.56,0.47	0.78,0.26
75	3.53,0.84	2.21,0.79	1.49,0.47	0.61,0.24
165	4.03,0.93	2.44,0.79	1.56,0.48	0.73,0.24
255	3.61,0.84	2.12,0.85	1.40,0.51	0.61,0.23
Avg.	3.8,0.95	2.3,0.79	1.5,0.48	0.68,0.24
R	4.500	3.625	3.200	2.380

[a] The first number is for ^{109}Cd and the second for ^{55}Fe.

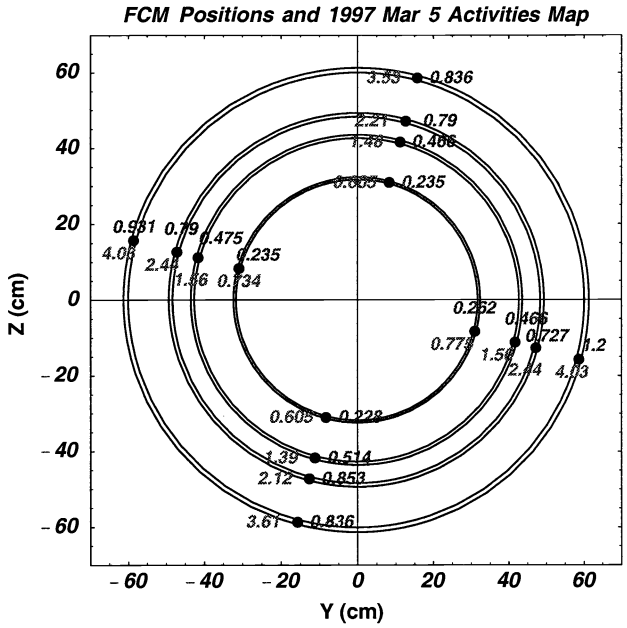

Figure 5. Positions of the FCM sources projected on the paraboloid apertures. The Y and Z axes are perpendicular to the optical axis and lie in the dispersion and cross-dispersion directions. The numbers are the ^{109}Cd and ^{55}Fe activities given in Table 1.

3. SPECTRAL ANALYSIS

The six readout CCDs for the I-array electronic configuration were all four I-array front-illuminated CCDs and the two central S-array CCDs S2 (front-illuminated) and S3 (back-illuminated), and for the S-array electronic configuration all six S-array CCDs (four front-illuminated and two, S1 and S3, back-illuminated). Figure 8 shows

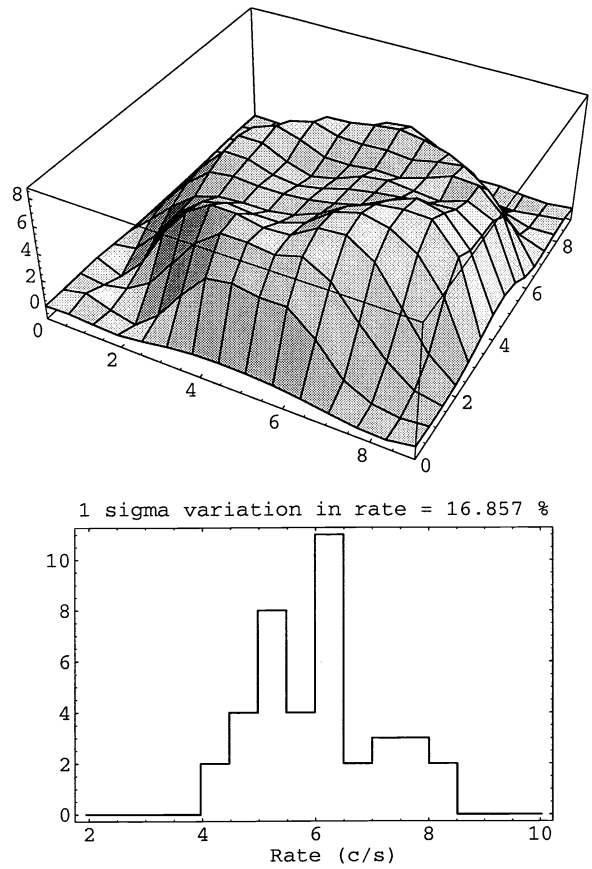

Figure 6. Uniformity measurement of a 9-mm diameter (shell 1) ^{109}Cd source at 3 keV (Ag Lα), using a CZT detector with a 1-mm aperture. The top panel is a surface plot of the measured rate; the bottom panel a histogram of the rate variation over the source.

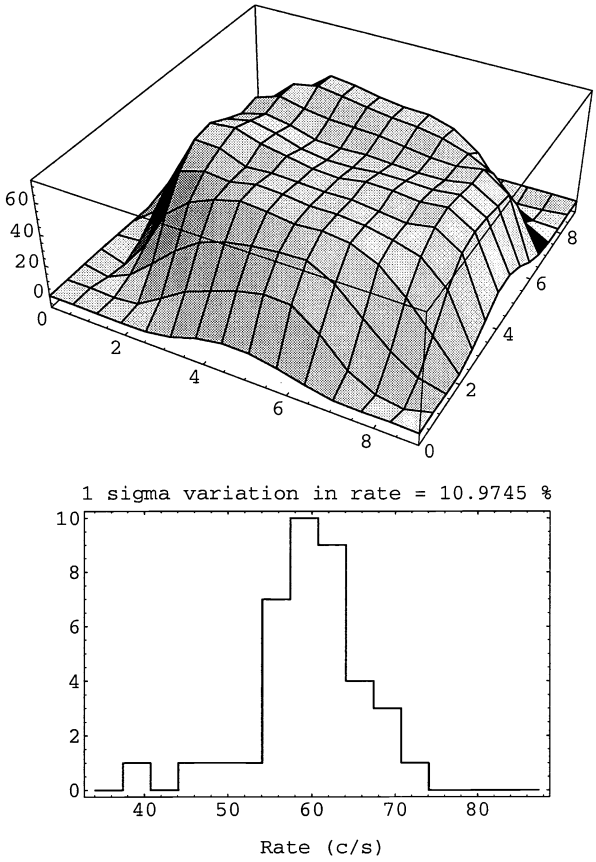

Figure 7. Uniformity measurement of a 9-mm diameter (shell 1) ^{55}Fe source at 6 keV (Mn Kα), using a CZT detector with a 1-mm aperture. The top panel is a surface plot of the measured rate; the bottom panel a histogram of the rate variation over the source.

the layout of the ACIS CCDs. Spectral analysis of FCM data taken at XRCF includes TRW IDs H-IAS-RC-1.001, H-IAS-RC-1.005, H-IAS-RC-1.004, and H-IAS-RC-1.002 for the I-array electronic configuration, and H-IAS-RC–8.001 for the S-array electronic configuration. RC-1.001 contains ~12,900 s of data. RC-1.005, RC-1.004, and RC-1.002 together contain ~ 7,600 s of data and so were combined. RC-8.001 contains only ~1,350 s of data, so the S-array configuration data from XRCF are of limited utility and, hence, excluded from the rest of our discussion. Spectral analysis of FCM data taken during OAC includes OBSIDs 62743 for the I-array configuration and 62742 for the S-array configuration. Longer integrations were necessary to compensate for radioactive decay of the FCM sources, so 62743 contains ~29,900 s of data and 62742 contains ~ 18,300 s of data. Regardless of the readout configuration, all data were obtained with the optical axis at the nominal S-array aim point (Fig. 8), and at XRCF with the ACIS detector at a position along the optical axis closest to the expected on-orbit position.

There were enough hot pixels to affect line fluxes only for on-orbit data from the S1 CCD. Due to different ACIS operating temperature, the number and locations of hot pixels differ for the OAC FCM, XRCF FCM, and flat-field data sets. We removed hot pixels from all CCDs using the following procedure. First, we define a pixel as hot if it was on in 5 percent of the frames in *any* of the data used. Second, we removed from analysis of *all* data sets those pixels identified as hot in any data set. Thus, we used exactly the same pixels in the analysis of the XRCF and OAC data. We correct for the tiny change in collecting area resulting from this procedure by using the same pixel set in the flat field. There are a population of pixels that are "warm" but on less than 5 percent of the time. The spectral distribution of events from these remaining warm pixels has no impact on the line flux measurements.

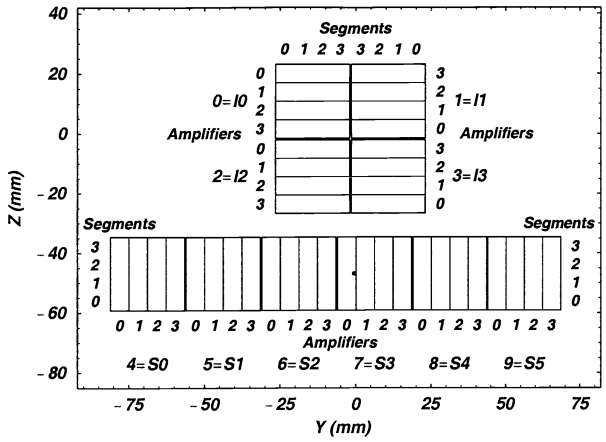

Figure 8. ACIS detector layout showing CCD, amplifier, and segment identifiers. The amplifiers are read out individually, and run horizontally for the I-array CCDs and vertically for the S-array CCDs. For the spectral and FCC position registration analysis, we divided each amplifier into 4 segments. Also shown by the black dot in amplifier 0 of CCD S3 is the position of the optical axis for the FCM measurements described in this paper.

We neglected the background under the lines in the XRCF data because it was so small. For the OAC data, we removed the much higher background using the data obtained when the aft contamination cover door was closed (OBSIDs 62708, 62707, and 62704 for the I-electronic configuration, and OBSIDs 62709 and 62906 for the S-electronic configuration). These data provide an excellent background for the OAC FCM data, as the only difference in the environment was the position of the aft contamination cover door.

There is a second, subtler effect arising from the background. Cosmic-ray tracks can affect a large number of pixels (mainly on the thicker front-illuminated CCDs). ACIS automatically detects and rejects these events, because either no local maximum is detected or, if there is a maximum, there is charge in all 8 pixels surrounding the maximum (*Chandra* grade 255). Any X rays superimposed on a cosmic-ray track are not detected. Thus cosmic ray tracks produce local areas on the detector that are temporarily dead. The impact is similar to an instrumental dead-time. We estimated the size of this effect using data collected on-orbit when ACIS is observing its external calibration source. We analyzed 98 data sets obtained at -110°C and, for each, determined the Mn-K line flux. We corrected for radioactive decay of the source and plotted our results versus the S3 CCD dropped amplitude rate. This rate, obtained once per frame per CCD, gives the number of events rejected onboard due to the pulse height exceeding the upper threshold. Because the back-illuminated CCDs are thinner than the front-illuminated CCDs, cosmic rays tend to affect fewer pixels, and so tend to be detected as large amplitude events. Thus the dropped amplitude events from S3 correlate with cosmic-ray flux. This analysis indicates that a typical on-orbit deadtime is 1.8±1.0 % for an front-illuminated CCD and 0.5±0.66 % for a back-illuminated CCD (68% statistical uncertainties).

We selected ASCA grades 0, 2, 3, 4 and 6 for further analysis. CCD grades reflect the distribution of detected charge and are useful for sorting real x-ray events from charged-particle tracks. Using the line list[6] given in Table 2, and after subtracting background and removing hot pixels, fits with four free parameters plus the norm for each line determine the rates in each line for each CCD, amplifier and segment (Fig. 8). The 96 data points per line resulting from this procedure are sufficient for determining FCC position shifts. Figure 9 shows the RC-1.001 spectra for a selected segment on the front-side-illuminated CCD I3 and one on the back-side-illuminated CCD S3. These segments lie near one another and above the optical axis (Fig. 8). The strongest lines in these spectra are the electron-capture lines Ag Lα, the Ag Lβ series, Mn Kα, and Mn Kβ1. Apparent from the figure is the superior energy resolution of the front-side-illuminated CCDs prior to the opening of the sunshade door and thus before the on-orbit degradation that occurred during radiation belt passages.[1] Comparison of XRCF line rates with those from OAC corrected for radioactive decay, ACIS dead time, and FCC position shifts, comprises the verification of the *Chandra* absolute flux calibration transfer and provides the basis for the search for any possible changes in molecular contamination.

4. FCM REGISTRATION ANALYSIS

In order to compare the FCM measurements at XRCF and OAC with each other and with ray-trace simulations, we must consider the following differences between XRCF and OAC:

(1) The FCM/FCC/HRMA and ACIS azimuthal orientation at XRCF differs by 180 degrees from that at OAC.

(2) The gravity environment at XRCF (one g with compensation) differs from that at OAC (zero g without compensation), leading to small changes in figure.

(3) The thermal environment at XRCF was about 30 °F (17 °C) warmer than at OAC, leading to different thermal contraction of the FCC holding the FCM.

Table 2. Line list for spectral fits.

Line	Energy (keV)	Line	Energy (keV)
(Ag Lα)[a]	1.2425	Ag Lγ1	3.5226
(Ag Lβ1)[a]	1.4111	Ag Lγ2	3.7432
Si-Kα	1.7398	(Mn Kα)[a]	4.1553
Au-Mα	2.1213	Mn Kα	5.8951
Au-Mβ	2.2050	Fe Kα	6.4000
Ag Lℓ	2.6637	Mn Kβ1	6.4904
Ag Lη	2.8061	Ni Kα	7.4724
Ag Lα	2.9823	Cu Kα	8.0411
Ag Lβ1	3.1509	Au Lℓ	8.4939
Ag Lβ6	3.2560	Au Lα	9.7130
Ag Lβ2	3.3478		

[a] Si K escape peak.

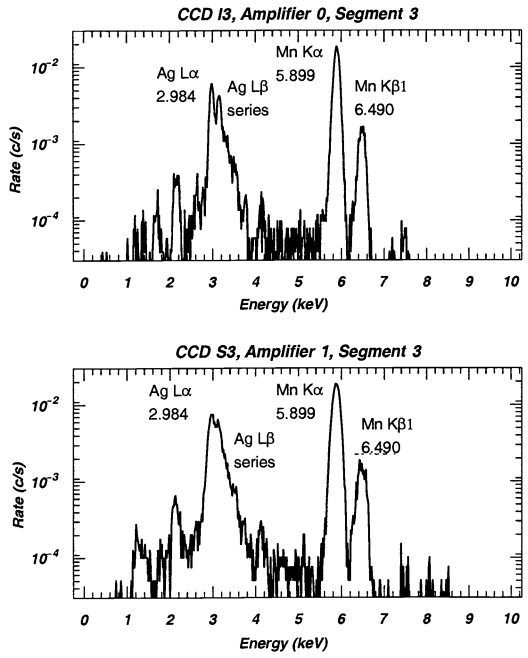

Figure 9. FCM/HRMA/ACIS spectra, from TRW ID H-IAS-RC-1.001, for a selected segment on the front-side-illuminated CCD I3 (top), and one on the back-side-illuminated CCD S3 (bottom).

(4) During XRCF testing, the FCC V-groove-block and cup-cone positioning mechanism was not properly aligned, and the magnitude of the resulting displacement, while visually estimated at <1 mm, mostly in Z, is not known accurately. Launch vibrations may also have contributed to changes in FCC positioning.

(5) Launch vibrations may have affected the relative positions of the FCM, FCC, and HRMA.

(6) The OAC rates must be corrected for radioactive decay and ACIS detector dead time.

Items (1)-(5) require registration of the FCM images from XRCF and OAC. By registration, we mean determining the position of the FCC relative to the HRMA, in order that the simulated images are correctly positioned on the ACIS detector. To do this we compare, by cross-correlation, measured images, flat fielded, at chosen line energies with simulated images. The simulations use the Kodak-measured FCM source positions on the FCC with respect to its nominal axis,[7] the as-built telescope model documented in the *Chandra* Mission Support Team calibration report, and the ray-trace code developed at MSFC,[8] for varying relative positions between the FCC and HRMA. We use the ACIS flat fields measured at XRCF. The ACIS operating temperature for the FCM measurements at OAC was 20 °F warmer than at XRCF, possibly affecting flat fielding, by affecting the CCD grade distribution. This additional source of systematic error is most relevant for the back-illuminated CCD S3. We carry out the cross-correlation registration analysis at the strongest lines, Ag Lα and Mn Kα (E = 2.984 and 5.899 keV, respectively), letting the overall normalizations for each CCD assume values that minimize the value of χ^2 at the various trial positions of the FCC. We also carry out the analysis at the rate weighted average energy of the Ag L line group (E $\simeq$ 3.198) and at Mn Kβ1 (E = 6.490 keV).

Although the ray-trace images generated using the Project Science ray-trace code appear to adequately reproduce the FCM images, in fact the best-fits are statistically unacceptable due to a variety of systematic effects that are difficult to take fully into account (see §5). We therefore constructed error contours, by rescaling χ^2 values to 1 per degree of freedom at the best-fit.[9] Fig. 10 shows the best-fit FCC position shifts at Ag Lα, the Ag Lβ group, Mn Kα and Mn Kβ1, together with 67% and 95% two-parameter error contours. While the FCC position did change from XRCF to OAC, it obviously cannot depend on energy. As shown in the figure, error contours for the four lines overlap in each case, as they must, and we now examine possible systematic errors in the predicted HRMA throughput at XRCF and OAC.

5. RATE CHANGES AND SYSTEMATIC ERRORS

FCM rates at OAC differ from the XRCF rates, due to the different circumstances listed in § 4, so we investigated sources of bias and systematic errors using our

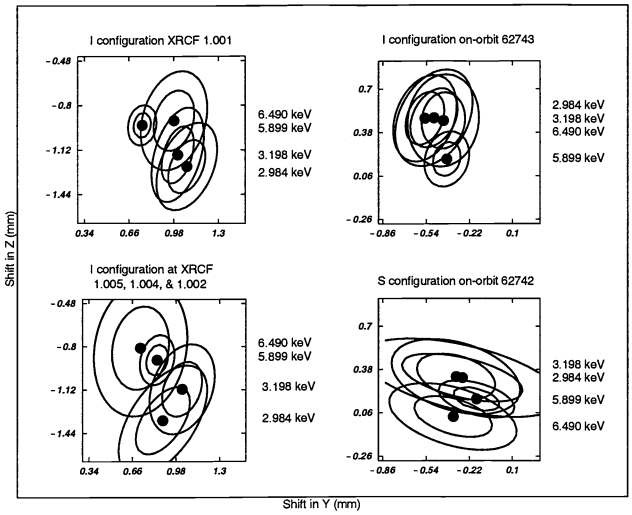

Figure 10. Best-fit values with error contours for the shift in FCC position from its nominal value relative to the HRMA. The lines show the 67% and 95% two parameter error contours.

ray-trace code. Table 3 presents the predicted change in I-configuration rates from XRCF to OAC, in the absence of molecular contamination. These predictions assume nominal values for the various relevant parameters, no radioactive decay, no ACIS dead time, and (for each CCD) a spatially uniform response at the energy dependent quantum efficiency given by tables available on the *Chandra* X-ray Center's calibration web pages (http://asc.harvard.edu/cal/).

Table 3. Predicted percent changes[a] in I configuration FCM rates from XRCF to OAC for nominal parameter values in the absence of molecular contamination.

CCDs	Ag Lα	Ag Lβ	Mn Kα	Mn Kβ
6[b]	+2.42	+2.43	+2.25	+1.93
3[c]	+1.58	+1.58	+1.35	+1.22

[a] $100(OAC_{nominal} - XRCF_{nominal})/OAC_{nominal}$. Statistical errors are $\sim 0.1\%$.

[b] I0+I1+I2+I3+S2+S3.

[c] I3+S2+S3.

In order to quantify various possible systematic errors, we varied parameters away from their nominal values and calculated the predicted changes from the nominal throughput. The results (Table 4) show that the largest systmatic effects are likely to come from registration errors and that the impact of systematic effects in general are reduced, but not eliminated, if consideration is restricted to the central region of the cross pattern in the focal plane. Indeed, Fig. 4 shows that gradients in the cross pattern are stronger in CCDs I0, I1 and I2 than in I3, S2 and S3. In addition, the second line in Table 3 shows that the apparent bias in the nominal results is reduced when the analysis is restricted to I3, S2, and S3.

Table 4. Systematic effects on predicted rate changes.

$\Delta T_{FCC} = \pm 5$ °F[a]	
I0+I1+I2+I3+S2+S3	±0.25 %
I3+S2+S3	±0.13 %
0.25 mm ACIS (Y,Z) displacements[b]	
I0+I1+I2+I3+S2+S3	±0.40 %
I3+S2+S3	±0.15 %
0.25 mm ACIS X displacements[c]	
I0+I1+I2+I3+S2+S3	±0.02 %
I3+S2+S3	±0.0025 %
Rotating HRMA by 180 degrees[d]	
I0+I1+I2+I3+S2+S3	±0.18 %
I3+S2+S3	±0.15 %
Different figure errors[e]	
I0+I1+I2+I3+S2+S3	+0.19 %
I3+S2+S3	+0.10 %
0.1 mm FCC (Y,Z) displacements[b]	
I0+I1+I2+I3+S2+S3	±0.61 %
I3+S2+S3	±0.34 %

[a] ± 5 °F changes in FCC temperature at either OAC or XRCF.

[b] The Y and Z axes are perpendicular to the optical axis.

[c] The X axis lies along the optical axis.

[d] The HRMA/ACIS azimuthal orientation at XRCF was 180 degrees from that at OAC.

[e] Calculated by applying the XRCF figure errors to OAC.

Predicted changes in FCM/HRMA/ACIS rate due to changes in molecular contamination from XRCF to OAC depend on the amount assumed to be present at XRCF, as shown in Fig. 11. The composition of the hydrocarbon layer assumed for these simulations was four hydrogen atoms for every carbon atom with a bulk density of 1 g/cm^3.

6. HRMA ABSOLUTE FLUX SCALE

Table 5 and Fig. 11 present the measured changes in total I-configuration rates (after correcting for radioactive de-

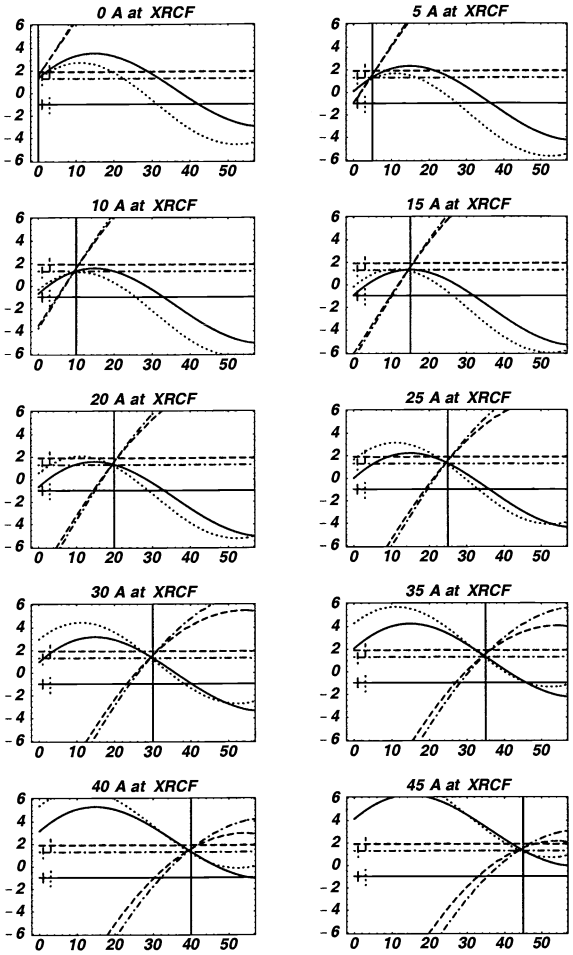

Figure 11. Measured (horizontal lines — for TRW ID H-IAS-RC-1.001) and predicted percent changes in I3+S2+S3 ACIS I-array electronic configuration rates from XRCF to OAC, at 2.984 (dash-dotted), 3.198 (dashed), 5.899 (solid), and 6.490 (dotted) keV, as a function of the thickness of a putative hydrocarbon layer at OAC. The different panels are for different assumed amounts of hydrocarbon present at XRCF. The vertical line extending from top to bottom of each panel marks zero change in thickness of the molecular film.

cay, flat fielding, and on-orbit dead time) from XRCF to OAC. **These results limit the absolute value of the change in mirror-detector system response to less than 2% at Ag L (~3 keV) and Mn K (~6 keV).**

The systematic effects discussed in §5 complicate the problem of setting limits on the total amounts of molecular contamination on the HRMA reflecting surfaces at XRCF and OAC. In addition, fitting the curves in Fig. 11 to the data in Table 5 results in a trough in χ^2 along the line of approximately equal thicknesses at XRCF and

Table 5. Percent change[a] in I-configuration FCM rates from XRCF to OAC (corrected for radioactive decay and ACIS dead time).

E	CCDs	1.001[b]	(5,4,2).001[c]	Wt. Avg.[d]
2.984	6[e]	0.95±0.80	0.73±0.86	0.85±0.41
	3[f]	1.84±1.06	0.68±1.16	1.31±0.55
3.198	6[e]	1.55±0.79	1.44±0.85	1.50±0.41
	3[f]	2.08±1.05	1.72±1.13	1.91±0.55
5.899	6[e]	-1.24±0.64	-0.85±0.66	-1.05±0.33
	3[f]	-1.30±0.79	-0.62±0.82	-0.97±0.40
6.490	6[e]	-0.93±1.13	-0.96±1.27	-0.95±0.60
	3[f]	-2.43±1.55	0.84±1.70	-0.94±0.81

[a] $100(OAC - XRCF)/OAC$.
Quoted errors are 1-σ statistical errors based on counts, dead-time uncertainties, and errors in the half-lives of the radioactive FCM sources, and do not include possible systematic contributions.

[b] XRCF data from TRW ID H-IAS-RC-1.001.

[c] XRCF data combined from TRW IDs H-IAS-RC-1.005, H-IAS-RC-1.004, and H-IAS-RC-1.002.

[d] Averages, weighted by square of errors, of previous two columns.

[e] I0+I1+I2+I3+S2+S3.

[f] I3+S2+S3.

OAC; the local minima in the trough are statistically indistinguishable according to the F-test and none are statistically acceptable at the 90% confidence level. However, we can get an idea of how much change there was from XRCF to OAC in the following way. From Fig. 1, we expect a rate of change in effective area at Ag Lα of 0.4% per Å of additional molecular contamination film thickness. Assuming a limit on the rate change at this line $\leq 2\%$ (see Table 5), we arrive at the conclusion that the change in effective thickness of a hydrocarbon film would be ≤ 10 Å. The predicted maximum change in thickness from XRCF to OAC was also 10 Å.[10]

Effective area measurements at XRCF,[3] together with results from the synchrotron reflectivity program,[11] suggest that the amount of molecular contamination at XRCF was small, probably < 13 Å. Based on those results, experience with the on-orbit performance, and the present analysis, we believe that only a small amount of molecular contamination was present on the HRMA at XRCF and at OAC.

7. ACKNOWLEDGEMENTS

We thank Terry Gaetz, Ping Zhao, Leon Van Speybroeck, and the SAO *Chandra* Mission Support Team as a whole, for their considerable help in understanding the as-built model for the HRMA. We thank SAO/Dale Graessle for sharing results from the synchrotron reflectivity program. We also thank TRW/Lorraine Ryan, TRW/Scott Texter, and Kodak/Fred Schwab for their help. Needless to say, the successful construction, launch, and operation of the *Chandra* X-ray Observatory resulted from the efforts of a very great number of dedicated people. We thank them all.

REFERENCES

1. M. C. Weisskopf, H. D. Tananbaum, L. P. Van Speybroeck, and S. L. O'Dell, "Chandra x-ray observatory: Overview," in *X-Ray Optics, Instruments, and Missions*, J. Trümper and B. Aschenbach, eds., *Proc. SPIE* **4012**, 2000.
2. M. C. Weisskopf and S. L. O'Dell, "Calibration of the AXAF observatory: Overview," in *Grazing Incidence and Multilayer X-Ray Optical Systems*, R. B. Hoover and A. B. Walker, eds., *Proc. SPIE* **3113**, pp. 2–17, 1997.
3. D. A. Schwartz, L. P. David, R. H. Donnelly, R. J. Edgar, T. J. Gaetz, D. Jerius, M. Juda, E. M. Kellogg, B. R. McNamara, P. P. Plucinsky, L. P. Van Speybroeck, B. J. Wargelin, S. Wolk, P. Zhao, D. Dewey, H. L. Marshall, N. S. Schulz, R. F. Elsner, J. J. Kolodziejczak, S. L. O'Dell, D. A. Swartz, A. F. Tennant, and M. C. Weisskopf, "Absolute effective area of the chandra high-resolution mirror assembly," in *X-Ray Optics, Instruments, and Missions*, J. Truemper and B. Aschenbach, eds., *Proc. SPIE* **4012**, pp. 28–40, 2000.
4. R. F. Elsner, M. K. Joy, S. L. O'Dell, B. D. Ramsey, and M. C. Weisskopf, "Ground-to-orbit transfer of the AXAF-I flux scale: In-situ contamination monitoring of x-ray telescopes," in *Multilayer and grazing incidence X-ray/EUV optics for astronomy and projection lithography*, R. B. Hoover and A. B. Walker, eds., *Proc. SPIE* **2279**, pp. 332–342, 1994.
5. T. W. Burrows, "The program radlist." Brookhaven National Laboratory Report BNL-NCS-52142 (http://www.nndc.bnl.gov/nndc/nudat/radform.html), February 29 1999.
6. J. A. Bearden, "X-ray wavelengths," *Rev. Mod. Phys.* **39**, pp. 78–124, 1967.
7. F. Schwab, "Radiation source position." Eastman-Kodak Tech Note No. AXAF-96-0251-SCHWAB, November 8 1997.
8. R. F. Elsner, S. L. O'Dell, B. D. Ramsey, A. F. Tennant, M. C. Weisskopf, J. J. Kolodziejczak, D. A. Swartz, D. E. Engelhaupt, G. P. Garmire, J. A. Nousek, M. W. Bautz, T. J. Gaetz, and P. Zhao, "Calibration results for the AXAF flight contamination monitor," in *X-Ray Optics, Instruments, and Missions*, R. B. Hoover and A. B. Walker, eds., *Proc. SPIE* **3444**, pp. 177–188, 1998.
9. W. H. Press, S. A. Teukolsky, W. T. Vetterling, and B. P. Flannery, *Numerical Recipes in FORTRAN, 2nd edition*, Cambridge University Press, Cambridge, 1992.
10. L. Ryan, "Chandra pre-ship mirror contamination levels." TRW document AXAF.99.200.003, January 27 1999.
11. D. E. Graessle, R. L. Blake, A. J. Burek, S. E. Dyson, J. J. Fitch, D. A. Schwartz, and R. Soufli, "Modeling of synchrotron reflectance measurements of AXAF iridium-coated witness mirrors over 2–12 keV," in *X-Ray Optics, Instruments, and Missions*, R. B. Hoover and A. B. Walker, eds., *Proc. SPIE* **3444**, pp. 140–159, 1998.